

Temperature enhancement of thermal Hall conductance quantization

I. C. Fulga,¹ Yuval Oreg,² Alexander D. Mirlin,^{3,4,5} Ady Stern,² and David F. Mross²

¹*IFW Dresden and Würzburg-Dresden Cluster of Excellence ct.qmat, Helmholtzstrasse 20, 01069 Dresden, Germany*

²*Department of Condensed Matter Physics, Weizmann Institute of Science, Rehovot 76100, Israel*

³*Institute for Quantum Materials and Technologies,*

Karlsruhe Institute of Technology, 76021 Karlsruhe, Germany

⁴*Institut für Theorie der Kondensierten Materie,*

Karlsruhe Institute of Technology, 76128 Karlsruhe, Germany

⁵*L. D. Landau Institute for Theoretical Physics RAS, 119334 Moscow, Russia*

(Dated: March 1, 2022)

The quest for non-Abelian quasiparticles has inspired decades of experimental and theoretical efforts, where the scarcity of direct probes poses a key challenge. Among their clearest signatures is a thermal Hall conductance with quantized half-integer value in natural units $\pi^2 k_B^2 T/3h$ (T is temperature, h the Planck constant, k_B the Boltzmann constant). Such a value was indeed recently observed in a quantum-Hall system and a magnetic insulator. We show that a non-topological ‘thermal metal’ phase that forms due to quenched disorder may disguise as a non-Abelian phase by well approximating the trademark quantized thermal Hall response. Remarkably, the quantization here *improves* with temperature, in contrast to fully gapped systems. We provide numerical evidence for this effect and discuss its possible implications for the aforementioned experiments.

Introduction—Measurements of the electronic or thermal Hall effect are among the most powerful experimental techniques for identifying topologically ordered phases and the nature of the fractional quasiparticles that they host [1]. An electronic Hall conductance that is sharply quantized to a non-integer value (in units of e^2/h , with e the electron charge) is intimately related to the existence of fractionally charged quasiparticles [2]. Similarly, a quantized non-integer thermal Hall conductance κ_{xy} (in units of $\kappa_0 = \pi^2 k_B^2 T/3h$) reflects excitations with non-Abelian braiding properties [3–8]. Unlike the electronic Hall effect, which has been routinely measured for several decades [9], precise measurements of the thermal Hall effect in solid-state systems have been achieved only recently [10–13]. Remarkably, experiments on two completely different systems found a half-integer value, which is indicative of so-called Ising anyons. The first of these is a two-dimensional electron gas in a perpendicular magnetic field at filling factor $\nu = 5/2$ with a thermal Hall conductance $\kappa_{xy} = 5/2$ [12]. The second is the layered magnetic insulator α -RuCl₃ where $\kappa_{xy} = 1/2$ per layer was measured in an applied magnetic field [13].

The level of quantization observed in the thermal Hall measurements is significantly below the one for their electronic analogues. This may be a consequence of heat leakage from the measured system to its environment, e.g., via phonons. Our work focuses on an additional, intrinsic property that may be particularly relevant to situations with half-integer κ_{xy} under experimental conditions, which necessarily include imperfections in the sample, i.e., disorder [14–16]. In the context of both the quantum Hall effect and α -RuCl₃, the half-integer κ_{xy} can be viewed as resulting from topological $p_x \pm ip_y$ pairing [3, 17] (and consequently chiral edge Majoranas) of *emergent* fermions: composite fermions and spinons, respectively. In both cases, the fermions are minimally coupled to an emergent gauge field, which acquires a

Higgs mass and thereby eliminates the phase mode of the emergent-fermion superconductor. The effective low-energy theory in both cases thus falls into class D in the Altland-Zirnbauer classification [18], which permits a delocalized *thermal metal* phase [5, 19–27]. This property is sharply distinct from, e.g., the symmetry class A of electrons in the quantum Hall effect, which always localizes unless the system is tuned to a topological phase transition [28]. The thermal metal also crucially differs from the metallic state formed from electrons that weakly anti-localize due to spin-orbit coupling [29–32]: It exhibits delocalized states only at energy $E = 0$ where particle-hole symmetry holds; at any non-zero energy it crosses over into class A at long length scales and all states eventually localize.

In this work we demonstrate that the localization characteristics of such systems have remarkable consequences: As temperature increases the longitudinal thermal conductance *decreases* and vanishes for a thermodynamically large system. Concomitantly, the thermal Hall conductance becomes better quantized. The reason for this somewhat counter-intuitive behavior is that thermal conductance is determined not solely by the delocalized $E = 0$ states, but by all states in an energy window $\sim T$. Since almost all of these states are localized, the thermal conductance vanishes. This localization behavior is similar to the one exhibited by electrons near an integer quantum Hall (IQH) plateau transition. There, an infinitely sharp transition at $T \neq 0$ is predicted on the single-particle level, but interactions render the width of the transition finite [33]. In the present case, interactions allow thermal metal behavior to persist over a finite temperature window. We will comment on the role of interactions and the differences between the IQH transition and the thermal metal towards the end of our discussion.

Model and symmetries—For concreteness, we will frame our discussion primarily in the language of the

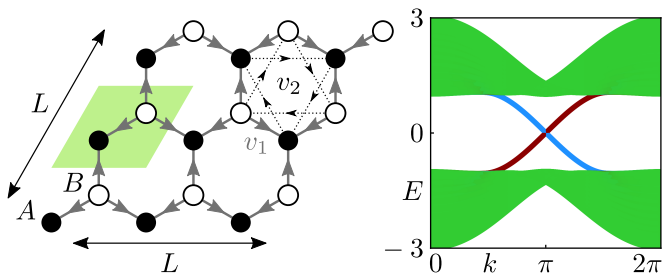


Figure 1. Left: The unit cell of the model (shaded area) contains two sites, indicated by filled and open circles, each hosting a single Majorana mode. The signs of (i times) the nearest-neighbor hopping v_1 and next-nearest-neighbor hoppings v_2 are indicated by the direction of arrows on the corresponding bonds. Right: Bandstructure of the model in a ribbon geometry, infinite in the horizontal direction and consisting of 30 unit cells in the vertical direction, using $v_1 = 1$ and $v_2 = -0.2$. Bulk states are shown in green, whereas states on the top and bottom edges are shown in red and blue, respectively.

quantum Hall plateau at $\nu = 5/2$. At energies below the charge gap, we model the system by a quadratic BdG Hamiltonian. To narrow down our choice of model, we require that it exhibits two topological phases that are related by time-reversal symmetry (TRS) and permits a thermal metal phase. (TRS of composite fermions corresponds to particle-hole symmetry of electrons within a single Landau level [34], which relates the Pfaffian and anti-Pfaffian phases [35, 36].)

A minimal model that satisfies these criteria is given by honeycomb lattice with a single Majorana fermion per site as shown in Fig. 1 [17]. (Such a model may also arise microscopically in the zero-flux sector of the Kitaev spin model.) The Hamiltonian reads

$$H = iv_1 \sum_{\langle j,k \rangle} \gamma_j \gamma_k + iv_2 \sum_{\langle\langle j,k \rangle\rangle} \gamma_j \gamma_k, \quad (1)$$

where γ_j is a Majorana operator on site j , $\langle j,k \rangle$ denotes directed bonds from a B to a neighboring A site, and $\langle\langle j,k \rangle\rangle$ clockwise next-nearest neighbor bonds (see Fig. 1). We set $v_1 = 1$ throughout the following, expressing all energy scales relative to it.

The Hamiltonian Eq. (1) obeys particle-hole (PH) symmetry. Writing $H = \gamma^T \mathcal{H} \gamma$, with γ a column vector of Majorana operators, the PH symmetry can be expressed as $\mathcal{H} = -\mathcal{H}^*$, such that the system belongs to class D. For $v_2 = 0$, the model features an additional TRS consisting of complex conjugation followed a sign-change of the wavefunction on one of the two sublattices, and thus falls into class BDI. Here, the spectrum is gapless, with two linearly dispersing Majorana cones at momenta K and K' . A non-zero mass term v_2 results in a gapped phase with Chern number $\mathcal{C} = \text{sgn}(v_2)$.

Notice that TRS, which is present for $v_2 = 0$, implies a vanishing thermal Hall conductance, while the corresponding particle-hole symmetry in the first excited

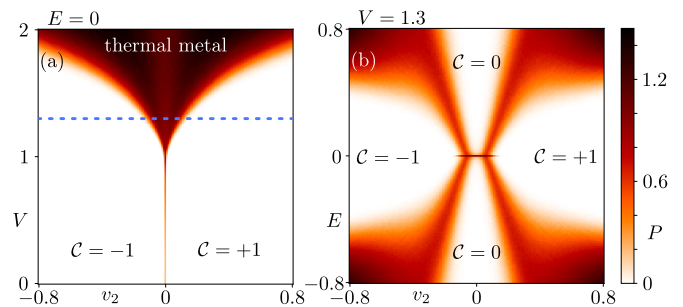


Figure 2. The average transmission of a 80×80 unit cells system, computed using 1000 disorder realizations. Panel a: the horizontal axis is v_2 and the vertical axis is disorder strength V . The topological transition between phases with Chern numbers $\mathcal{C} = \pm 1$ evolves into an extended thermal metal phase with increasing disorder strength. The dashed blue line indicates $V = 1.3$. Panel b: for fixed $V = 1.3$, the average transmission is plotted as a function of v_2 and energy E . Away from the particle-hole symmetric line $E = 0$, the thermal metal phase disappears; it is replaced by topologically trivial insulators ($\mathcal{C} = 0$).

Landau level requires the value $5/2$ [37]. Consequently, a ‘background’ contribution of $5/2$ must be added to interpret results for the model system above in the quantum Hall context, i.e., $\kappa_{xy}^{\text{QH}} = \kappa_{xy} + 5/2$. The TRS breaking parameter v_2 may be viewed as describing either Landau level mixing or the deviations of ν from $5/2$.

Zero-temperature phase diagram—We now introduce random hopping disorder and examine the localization properties near the topological phase transition of the clean system as a function of disorder strength V and energy E . Specifically, we replace $v_i \rightarrow v_i + \delta v_i$ with δv_1 from a uniform distribution $[-V, V]$ and δv_2 from $[-V/10, V/10]$. We numerically compute the energy-dependent transmission probability $P(E)$ for a cylindrical $L \times L$ system with zig-zag edges. [See Supplemental Material for details of the calculation].

In Fig. 2(a) we show the transmission at zero energy, $P(E = 0)$ as a function of v_2 and disorder strength. At weak disorder, the insulating phases with $\mathcal{C} = \pm 1$ remain separated by a direct plateau transition, see also discussion in Refs. [19, 23–26]. When $V \gtrsim 1$, however, a delocalized phase develops in the vicinity of $v_2 = 0$. This is a disorder-induced thermal metal where $P(E = 0)$ increases logarithmically with system size (see Supplemental Material). Further increasing the disorder strength enlarges the thermal metal region of the phase diagram. In Fig. 2(b), we plot the energy-dependent transmission probability at fixed disorder strength $V = 1.3$, for which the thermal metal phase is well-developed. We observe that the metal is only present at $E = 0$. This is the expected result based on weak anti-localization in the PH symmetric case, $E = 0$, and weak localization for any $E \neq 0$. The latter case features direct insulator-to-insulator transitions, with trivial, $\mathcal{C} = 0$ phases appearing between the topological phases with $\mathcal{C} = \pm 1$.

We have further observed that the crossover regions in Fig. 2(b) (the regions where transmission is non-zero) shrink with increasing system size and grow with δv_2 disorder. The former is required due to the absence of metallic phases in class A, i.e., for $E \neq 0$. To understand the latter, recall that for $v_2 = \delta v_2 = 0$ the model is in class BDI, which only permits a critical-metal phase (without anti-localization), distinct from the class-D thermal metal [25]. Gradually introducing δv_2 disorder allows the formation of a growing thermal metal phase at $E = 0$ and, in finite systems, a corresponding crossover at $E \neq 0$. For the system sizes we can access numerically, we find that the $C = 0$ insulator fully disappears into a smooth crossover for approximately equal v_1 and v_2 disorder.

At $E \neq 0$ the system is in class A and thus always localizes. For small energies, the localization length is determined by the crossover between weak anti-localization of class D and weak localization of class A [24]. At distances smaller than the diffusion length $L_E = \sqrt{D/E}$, with D the diffusion constant, the interference of electron and hole trajectories gives rise to a logarithmic increase of the conductance. At scales larger than L_E , this interference is suppressed; the system behaves as a class A conductor, which tends to localize beyond a localization length $\xi(E)$. The latter can be computed as for the case of spin-orbit coupled electrons in a weak magnetic field, which features a similar crossover between weakly anti-localizing class AII and weakly localizing class A [38]. We find

$$\xi(E) = \frac{\ell_0}{\sqrt{E}} \exp\left(\frac{1}{4} \ln^2 \frac{1}{E}\right), \quad (2)$$

with ℓ_0 the mean free path (see Supplemental Material for details). Both $L_E, \xi(E)$ depend on energy and diverge with decreasing energy, with asymptotically $\xi(E) \gg L_E$. In a finite-size system it is further useful to define two crossover energy scales: $E_L \propto L^{-2}$, for which $L_E = L$, and E_c , for which $\xi = L$. States with energies below E_L are weakly anti-localizing, states with energies between E_L and E_c are characterized by weak localization, whereas strong localization sets in above E_c .

Finite temperature effects—The above discussion and the results presented in Fig. 2 suggest that the dimensionless thermal conductance tensor κ changes qualitatively as temperature is swept past either crossover scale. (In an infinite system $E_c = E_L = 0$.) To test this expectation we compute κ_{xx} and κ_{xy} in a six-terminal transport geometry, where both can be obtained in the same numerical simulation. Terminals are numbered from 1 to 6, as shown in the inset of Fig. 3 (see Supplemental Material). The scattering matrix has a 6×6 block structure, with blocks \mathfrak{s}_{ij} containing the probability amplitudes for transmission from lead i to lead j .

All reservoirs are kept at the same chemical potential, and terminals 1 and 4 are temperature biased as $T_{1,4} = \pm \Delta T/2$ relative to the base temperature T of the system. Consequently there is a heat current $I_Q = I_1 = -I_4$

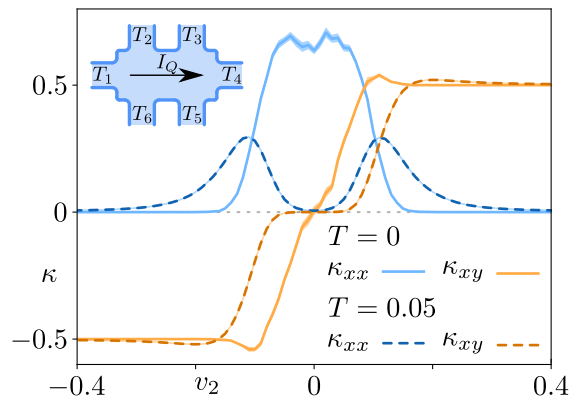


Figure 3. The dimensionless longitudinal and transverse thermal conductances (blue, orange) are computed in a six-terminal geometry (inset) at $T = 0$ and $T = 0.05$ (solid, dashed). We use a rectangular system composed of 80 zig-zag chains in the vertical direction and 160 hexagonal plaquettes in the horizontal direction, and average over 1000 disorder realizations ($V = 1.3$), with line thickness indicating the error bars. The thermal metal phase present in the $v_2 = 0$ region of the plot is converted into an insulating phase at non-zero temperature, leading to a quantized plateau in both longitudinal and transverse conductance. Notice the smaller error bars in the finite-temperature curves, which occur because the energy integral Eq. (4) provides additional disorder averaging.

through the system. The remaining terminals are connected to thermometers, such that $I_{2,3,5,6} = 0$. Setting $h = k_B = 1$, temperatures and heat current are related via [39]

$$\begin{pmatrix} I_Q \\ 0 \\ 0 \\ -I_Q \\ 0 \\ 0 \end{pmatrix} = M \begin{pmatrix} \Delta T/2 \\ T_2 \\ T_3 \\ -\Delta T/2 \\ T_5 \\ T_6 \end{pmatrix}, \quad (3)$$

where the matrix M is given by

$$M_{ij} = \int_0^\infty \frac{E^2}{T} \left(-\frac{\partial f(E, T)}{\partial E} \right) \left[\delta_{ij} N_j - \text{tr}(\mathfrak{s}_{ij}^\dagger \mathfrak{s}_{ij}) \right] dE, \quad (4)$$

with δ_{ij} denoting the Kronecker delta, N_j the number of modes in lead j and $f(E, T) = 1/(1 + e^{E/T})$ the Fermi-Dirac distribution at temperature T . Notice that the scattering matrix depends on energy, which results in a non-trivial temperature dependence of M . We numerically compute the matrix M for each disorder realization, and insert it into Eq. (3) to compute the elements of the thermal resistance tensor, R_{xx} and R_{xy} . We define $R_{xx} = (T_2 - T_3)/I_Q$, whereas for R_{xy} we average over the temperature drop between terminals 2 and 6 and between terminals 3 and 5: $R_{xy} = (T_2 - T_6 + T_3 - T_5)/(2I_Q)$. This is done in order to reduce geometric effects which would otherwise lead to an asymmetry in the plots. The dimensionless conductance tensor κ is then obtained by invert-

ing R and dividing by κ_0 . In Fig. 3 we plot the disorder-averaged components κ_{xx} and κ_{xy} at $T = 0$ (solid lines) and $T = 0.05$ (dashed lines).

To understand the observed behavior, notice that temperature-dependent factor in the integrand of Eq. (4) is sharply peaked at energies around T and becomes a delta function at zero temperature. For temperatures below the crossover energy scale E_c , the main contribution to the integral comes from extended states and κ_{xx} is large while κ_{xy} is approximately linear in v_2 . The low-temperature regime subdivides into $T < E_L$, where κ_{xx} is determined by the metallic transmission probability $P(E \approx 0)$ and $E_L < T < E_c$, where weak localization corrections modify this result (see Supplemental Material). At temperatures above E_c , strong localization becomes operative and leads to $\kappa_{xx} \rightarrow 0$, as we observe numerically. This insulating behavior is accompanied by an emergent intermediate plateau in κ_{xy} , as shown in Fig. 3 and Fig. 4(a).

Effect of interactions—Both the numerical simulations and the σ -model treatment were performed within quadratic fermionic Hamiltonians, where transport is fully phase-coherent. We now qualitatively discuss how interactions change these results, focusing on the fractional quantum Hall effect at $\nu = 5/2$. We consider a thermodynamically large system, $L \rightarrow \infty$, and focus mostly on phase-breaking of the emergent fermions. The presence of phonons leads to another channel for heat transport, which is expected to follow a power-law of $\kappa^{ph} \propto T^5$ [40]. Its contribution is suppressed at low temperatures, as indeed observed in the experiment [12, 13].

The phase-breaking interactions of an interfering particle with its environment introduce a dephasing length L_ϕ [41], which diverges with decreasing temperature, presumably following a power law. This length should be compared to two other length scales defined above [near Eq. (2)]: the diffusion length L_E and the localization length $\xi(E)$. Here, the relevant energy is the temperature, since the chemical potential is pinned to zero.

For a clean sample at high temperature, the dephasing length is presumably the shortest scale, and the system's conductance takes the anti-localizing class D form, where $\kappa_{xx} \propto \log L_\phi/\ell_0$. As the temperature is lowered, we will have $L_\phi > L_E$. Then, patches of size L_ϕ become large enough for each patch to manifest a tendency to localization as a system of class A. Thus, in this regime, the conductance decreases with decreasing temperature, with its maximum $\log(D/T\ell_0^2)$ being attained when $L_\phi \approx \sqrt{D/T}$. If phase-breaking is sufficiently weak, there will be an intermediate range of temperatures in which $L_\phi > \xi$; in this regime we expect a conductance much smaller than unity. The charge-neutrality of the Majorana particles suggests that such a regime may indeed exist. In any case, in the zero-temperature limit the energy dependence of ξ [see Eq. (2)] makes it larger than L_ϕ and the system becomes metallic.

Conclusion—We have shown that in systems whose effective low-energy theory falls into symmetry class D,

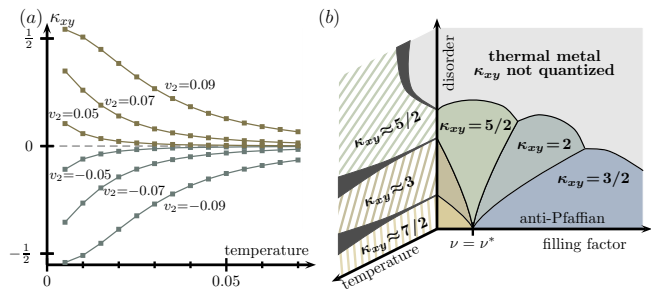


Figure 4. (a) The numerically computed thermal conductance shows order-unity variations with v_2 at low temperatures. At higher temperatures it approaches the time-reversal symmetric value $\kappa_{xy} = 0$ with very weak dependence on $v_2 \in [-0.07, 0.07]$. (b) Proposed finite-temperature phase diagram of $\nu \approx 5/2$ quantum Hall states based on our findings. The thermal metal extends to finite temperatures due to residual interactions between neutral quasiparticles. At higher temperatures, but still below the charge gap, the mechanism discussed here sets in. In the vicinity of ν^* it results in a large region where κ_{xy} approaches the particle-hole symmetric value $5/2$. Hatched regions denote quantization of κ_{xy} that is better than a threshold value, say 1%. The approximate plateaus are separated by relatively sharp crossovers as shown in Fig. 3.

increasing temperature can *enhance* quantization of the thermal Hall response. Moreover, new plateaus of quantized κ_{xy} that are absent in the low-temperature limit may emerge and exhibit near-perfect quantization. These findings have direct implications for the interpretation of the measured half-integer values of κ_{xy} in Refs. [12, 13].

In the context of the $\nu = 5/2$ plateau, it is not settled whether the observed thermal Hall conductance represents a true bulk property or is due to incomplete equilibration between edge states [42–46]. In the former case, the PH-Pfaffian phase with topologically quantized $\kappa_{xy} = 5/2$, a disorder-induced topological phase with the same quantized value, or a thermal metal where κ_{xy} is not strictly quantized are all possible [14–16]. If particle-hole symmetry were present, it would constrain the Hall response of the thermal metal to be the same as that of PH-Pfaffian. In reality, this symmetry is broken due to relatively strong mixing between Landau levels – the Coulomb energy is comparable to the Landau level splitting in the relevant experiments. Our work shows how an approximately quantized thermal Hall response can emerge with increasing temperature out of a zero-temperature thermal metal whose response is non-quantized. We thus propose that the zero-temperature phase diagram of the quantum Hall state near $\nu = 5/2$ introduced in Refs. [14–16] extends to non-zero temperatures as shown in Fig. 4(b).

More generally, our work emphasizes the importance of systematically measuring the temperature dependence of the approximately quantized κ_{xy} . (In the case of α -RuCl₃ the thermal Hall measurements were performed at moderately large temperatures of around 4

Kelvin.) Theoretically, a careful analysis of dephasing could help determine whether an underlying thermal metal is a possibility or if the measured κ_{xy} reflects a topological phase.

ACKNOWLEDGMENTS

It is a pleasure to thank Olexei Motrunich, Anton Akhmerov, and Moty Heiblum for illuminating discussions on this topic, and Ulrike Nitzsche for technical assistance. This work was partially supported by the

Deutsche Forschungsgemeinschaft (DFG, German Research Foundation) under Germany's Excellence Strategy through the Würzburg-Dresden Cluster of Excellence on Complexity and Topology in Quantum Matter – *ct.qmat* (EXC 2147, project-id 390858490), through CRC/Transregio 183, and through grants EI 519/7-1 and MI 658/10-1, by the ERC under the European Unions Horizon 2020 research and innovation programme (grant agreement LEGOTOP No 788715), the BSF and NSF (2018643), the ISF (1866/17), the ISF Quantum Science and Technology (2074/19), and by the German-Israeli Foundation (grant I-1505-303.10/2019).

-
- [1] C. L. Kane and Matthew P. A. Fisher, “Quantized thermal transport in the fractional quantum Hall effect,” *Phys. Rev. B* **55**, 15832–15837 (1997).
 - [2] D. Arovas, J. R. Schrieffer, and F. Wilczek, “Fractional statistics and the quantum Hall effect,” *Phys. Rev. Lett.* **53**, 722–723 (1984).
 - [3] G. Moore and N. Read, “Nonabelions in the fractional quantum Hall effect,” *Nucl. Phys. B* **360**, 362–396 (1991).
 - [4] N. Read and E. Rezayi, “Beyond paired quantum Hall states: Parafermions and incompressible states in the first excited Landau level,” *Phys. Rev. B* **59**, 8084–8092 (1999).
 - [5] N. Read and D. Green, “Paired states of fermions in two dimensions with breaking of parity and time-reversal symmetries and the fractional quantum Hall effect,” *Phys. Rev. B* **61**, 10267–10297 (2000).
 - [6] A. Cappelli, M. Huerta, and G. R. Zemba, “Thermal transport in chiral conformal theories and hierarchical quantum Hall states,” *Nucl. Phys. B* **636**, 568–582 (2002).
 - [7] B. A. Bernevig and F. D. M. Haldane, “Properties of non-Abelian fractional quantum Hall states at filling $\nu = k/r$,” *Phys. Rev. Lett.* **101**, 246806 (2008).
 - [8] A. Gromov, G. Y. Cho, Y. You, A. G. Abanov, and E. Fradkin, “Framing anomaly in the effective theory of the fractional quantum Hall effect,” *Phys. Rev. Lett.* **114**, 016805 (2015).
 - [9] K. v. Klitzing, G. Dorda, and M. Pepper, “New method for high-accuracy determination of the fine-structure constant based on quantized Hall resistance,” *Phys. Rev. Lett.* **45**, 494–497 (1980).
 - [10] S. Jezouin, F. D. Parmentier, A. Anthore, U. Gennser, A. Cavanna, Y. Jin, and F. Pierre, “Quantum limit of heat flow across a single electronic channel,” *Science* **342**, 601–604 (2013).
 - [11] M. Banerjee, M. Heiblum, A. Rosenblatt, Y. Oreg, D. E. Feldman, A. Stern, and V. Umansky, “Observed quantization of anyonic heat flow,” *Nature* **545**, 75–79 (2017).
 - [12] M. Banerjee, M. Heiblum, V. Umansky, D. E. Feldman, Y. Oreg, and A. Stern, “Observation of half-integer thermal Hall conductance,” *Nature* **559**, 205–210 (2018).
 - [13] Y. Kasahara, T. Ohnishi, Y. Mizukami, O. Tanaka, S. Ma, K. Sugii, N. Kurita, H. Tanaka, J. Nasu, Y. Motome, T. Shibauchi, and Y. Matsuda, “Majorana quantization and half-integer thermal quantum Hall effect in a Kitaev spin liquid,” *Nature* **559**, 227–231 (2018).
 - [14] D. F. Mross, Y. Oreg, A. Stern, G. Margalit, and M. Heiblum, “Theory of disorder-induced half-integer thermal Hall conductance,” *Phys. Rev. Lett.* **121**, 026801 (2018).
 - [15] C. Wang, A. Vishwanath, and B. I. Halperin, “Topological order from disorder and the quantized Hall thermal metal: Possible applications to the $\nu = 5/2$ state,” *Phys. Rev. B* **98**, 045112 (2018).
 - [16] B. Lian and J. Wang, “Theory of the disordered $\nu = \frac{5}{2}$ quantum thermal Hall state: Emergent symmetry and phase diagram,” *Phys. Rev. B* **97**, 165124 (2018).
 - [17] A. Kitaev, “Anyons in an exactly solved model and beyond,” *Ann. Phys.* **321**, 2–111 (2006).
 - [18] A. Altland and M. R. Zirnbauer, “Nonstandard symmetry classes in mesoscopic normal-superconducting hybrid structures,” *Phys. Rev. B* **55**, 1142–1161 (1997).
 - [19] S. Cho and M. P. A. Fisher, “Criticality in the two-dimensional random-bond Ising model,” *Phys. Rev. B* **55**, 1025–1031 (1997).
 - [20] T. Senthil, M. P. A. Fisher, L. Balents, and C. Nayak, “Quasiparticle transport and localization in high- T_c superconductors,” *Phys. Rev. Lett.* **81**, 4704–4707 (1998).
 - [21] T. Senthil and M. P. A. Fisher, “Quasiparticle localization in superconductors with spin-orbit scattering,” *Phys. Rev. B* **61**, 9690–9698 (2000).
 - [22] M. Bocquet, D. Serban, and M. R. Zirnbauer, “Disordered 2d quasiparticles in class D: Dirac fermions with random mass, and dirty superconductors,” *Nuclear Physics B* **578**, 628–680 (2000).
 - [23] J. T. Chalker, N. Read, V. Kagalovsky, B. Horovitz, Y. Avishai, and A. W. W. Ludwig, “Thermal metal in network models of a disordered two-dimensional superconductor,” *Phys. Rev. B* **65**, 012506 (2001).
 - [24] A. Mildenberger, F. Evers, A. D. Mirlin, and J. T. Chalker, “Density of quasiparticle states for a two-dimensional disordered system: Metallic, insulating, and critical behavior in the class-D thermal quantum Hall effect,” *Phys. Rev. B* **75**, 245321 (2007).
 - [25] F. Evers and A. D. Mirlin, “Anderson transitions,” *Rev. Mod. Phys.* **80**, 1355–1417 (2008).
 - [26] V. Kagalovsky and D. Nemirovsky, “Critical fixed points in class D superconductors,” *Phys. Rev. B* **81**, 033406 (2010).
 - [27] C. R. Laumann, A. W. W. Ludwig, D. A. Huse, and S. Trebst, “Disorder-induced Majorana metal in interacting non-Abelian anyon systems,” *Phys. Rev. B* **85**,

- 161301 (2012).
- [28] B. Kramer and A. MacKinnon, “Localization: theory and experiment,” *Repr. Prog. Phys.* **56**, 1469–1564 (1993).
- [29] S. Hikami, A. I. Larkin, and Y. Nagaoka, “Spin-orbit interaction and magnetoresistance in the two dimensional random system,” *Prog. Theor. Phys.* **63**, 707–710 (1980).
- [30] Y. Asada, K. Slevin, and T. Ohtsuki, “Anderson transition in two-dimensional systems with spin-orbit coupling,” *Phys. Rev. Lett.* **89**, 256601 (2002).
- [31] Y. Asada, K. Slevin, and T. Ohtsuki, “Numerical estimation of the β function in two-dimensional systems with spin-orbit coupling,” *Phys. Rev. B* **70**, 035115 (2004).
- [32] H. Obuse, A. Furusaki, S. Ryu, and C. Mudry, “Two-dimensional spin-filtered chiral network model for the F_2 quantum spin-Hall effect,” *Phys. Rev. B* **76**, 075301 (2007).
- [33] Z. Wang, M. P. A. Fisher, S. M. Girvin, and J. T. Chalker, “Short-range interactions and scaling near integer quantum Hall transitions,” *Phys. Rev. B* **61**, 8326–8333 (2000).
- [34] D. T. Son, “Is the composite fermion a Dirac particle?” *Phys. Rev. X* **5**, 031027 (2015).
- [35] S.-S. Lee, S. Ryu, C. Nayak, and M. P. A. Fisher, “Particle-hole symmetry and the $\nu = 5/2$ quantum hall state,” *Phys. Rev. Lett.* **99**, 236807 (2007).
- [36] M. Levin, B. I. Halperin, and B. Rosenow, “Particle-Hole Symmetry and the Pfaffian State,” *Phys. Rev. Lett.* **99**, 236806 (2007).
- [37] Neither symmetry is related to the intrinsic PH symmetry of BdG Hamiltonians, which does not impose any such constraint.
- [38] I. V. Lerner and Y. Imry, “Magnetic-field dependence of the localization length in Anderson insulators,” *Europhys. Lett.* **29**, 49–54 (1995).
- [39] W. Long, H. Zhang, and Q.-F. Sun, “Quantum thermal Hall effect in graphene,” *Phys. Rev. B* **84**, 075416 (2011).
- [40] J. M. Ziman, *Electrons And Phonons: The Theory of Transport Phenomena in Solids (Oxford Classic Texts in the Physical Sciences)* (Oxford University Press, U.S.A., 2001).
- [41] Y. Imry, *Introduction to mesoscopic physics* (Oxford University Press, New York, 1997).
- [42] S. H. Simon, “Interpretation of thermal conductance of the $\nu = 5/2$ edge,” *Phys. Rev. B* **97**, 121406 (2018).
- [43] K. K. W. Ma and D. E. Feldman, “Partial equilibration of integer and fractional edge channels in the thermal quantum Hall effect,” *Phys. Rev. B* **99**, 085309 (2019).
- [44] S. H. Simon and B. Rosenow, “Partial equilibration of the anti-Pfaffian edge due to Majorana disorder,” *Phys. Rev. Lett.* **124**, 126801 (2020).
- [45] H. Asasi and M. Mulligan, “Partial equilibration of anti-Pfaffian edge modes at $\nu = 5/2$,” arXiv e-prints, arXiv:2004.04161 (2020), arXiv:2004.04161 [cond-mat.str-el].
- [46] J. Park, C. Spänslätt, Y. Gefen, and A. D. Mirlin, “Noise on the non-Abelian $\nu = 5/2$ fractional quantum Hall edge,” arXiv e-prints, arXiv:2006.06018 (2020), arXiv:2006.06018 [cond-mat.mes-hall].

Supplemental Material to: “Temperature enhancement of thermal Hall conductance quantization”

I. C. Fulga,¹ Yuval Oreg,² Alexander D. Mirlin,^{3,4,5} Ady Stern,² and David F. Mross²

¹*IFW Dresden and Würzburg-Dresden Cluster of Excellence ct.qmat, Helmholtzstrasse 20, 01069 Dresden, Germany*

²*Department of Condensed Matter Physics, Weizmann Institute of Science, Rehovot 76100, Israel*

³*Institute for Quantum Materials and Technologies,*

Karlsruhe Institute of Technology, 76021 Karlsruhe, Germany

⁴*Institut für Theorie der Kondensierten Materie,*

Karlsruhe Institute of Technology, 76128 Karlsruhe, Germany

⁵*L. D. Landau Institute for Theoretical Physics RAS, 119334 Moscow, Russia*

(Dated: March 1, 2022)

In this Supplemental Material we provide details on the transport geometry used to determine the thermal conductance and show numerically obtained conductance scaling plots. In addition, we estimate energy dependence of the localization length both numerically and by using a non-linear σ model approach.

I. TRANSPORT GEOMETRY

All numerical simulations are performed using the Kwant code [1]. In the two-terminal geometry, we use a square shaped system consisting of $L \times L$ unit cells, with periodic boundary conditions in the horizontal direction. Ideal leads are attached to the top- and bottom-most unit cells of the system and are modeled as ‘doped’ Kitaev models. The lead Hamiltonian has the same form as in the main text (with $v_2 = 0$), except that it is considered to describe spinless, complex fermions instead of Majorana modes. The doping then corresponds to a global shift of the Fermi level: $\mathcal{H} \rightarrow \mathcal{H} + 0.5v_1$, which breaks particle-hole symmetry. These leads are connected to fermionic reservoirs that are held at identical electrochemical potential but different temperatures. The resulting scattering matrix,

$$S = \begin{pmatrix} \mathbf{r} & \mathbf{t}' \\ \mathbf{t} & \mathbf{r}' \end{pmatrix}, \quad (1)$$

is composed of blocks $\mathbf{r}^{(l)}$ and $\mathbf{t}^{(l)}$ containing the probability amplitudes for lead modes to be back-reflected or transmitted across the system, respectively. As mentioned in the main text, this allows us to determine the transmission probability through the system as $P(E) = \text{tr}(\mathbf{t}^\dagger \mathbf{t})$. Notice that this total transmission probability includes a sum over transmissions of a fermion emanating from one reservoir to a fermion that is absorbed in another reservoir. The fermions can be either electrons or holes, as all processes transfer energy between the reservoirs. The use of leads and reservoirs here should be viewed as a computational vehicle allowing us to probe theoretically the localization properties of the system’s bulk. The modeling of the hot and cold reservoirs and the leads in actual experiments are more involved, but that should not affect significantly the bulk properties and their temperature dependence that we study here.

To determine the longitudinal thermal conductance in the two-terminal geometry, we assume that the fermionic reservoirs are kept at the same chemical potential. In-

stead, the reservoirs are temperature biased by an amount $\pm\Delta T/2$ relative to the temperature T of the superconductor. As such, a heat current I_Q flows through the device, leading to a longitudinal thermal conductance $\kappa_0 \kappa_{xx} = I_Q/\Delta T$, which in linear response reads

$$\kappa_{xx}(T) = \frac{1}{T\kappa_0} \int_0^\infty E^2 \left(-\frac{\partial f(E,T)}{\partial E} \right) P(E) dE. \quad (2)$$

Here, $f(E,T) = (1 + \exp(E/T))^{-1}$ is the Fermi function at temperature T , relative to the Fermi level $E_F = 0$, and we have set $\hbar = k_B = 1$. In the limit of zero temperature, $T \rightarrow 0$, Eq. (2) yields a dimensionless conductance $\kappa_{xx} = P(E=0)$.

In the six terminal geometry, we consider a rectangular system composed of 80 zig-zag chains in the vertical direction and 160 hexagonal plaquettes in the horizontal direction. The six leads are positioned symmetrically with respect to each edge of the system, as sketched in the inset of Fig. 3 of the main text. In the six terminal setup, the lead Hamiltonian is formed out of decoupled Kitaev chains at their critical point (hopping strength equal to v_1), with each chain connecting to one site of the system.

II. CONDUCTANCE SCALING

As shown in the left panel of Fig. 1, in the limit of zero temperature the thermal metal phase is characterized by a logarithmic scaling of conductance with system size, as expected for weak anti-localization. The fit to $\ln L$ yields a slope ~ 0.26 , close to the predicted value of $1/\pi$ [2]. At finite temperatures, however, we observe that the conductance decreases with system size instead, as shown in the right panel of Fig. 1. Since the disorder average commutes with the energy integral of Eq. (2), we determine the finite temperature κ_{xx} by first averaging the transmission probability over disorder, and then numerically evaluating the energy integral. At nonzero

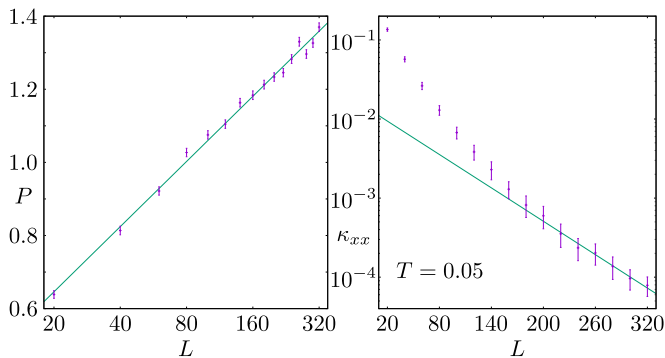


Figure 1. Left panel: the average transmission at $E = 0$ is plotted versus system size setting $v_2 = 0$ and $V = 1.3$. Notice the log scale on the horizontal axis. The solid line shows a logarithmic increase, expected for a thermal metal. Right panel: the average dimensionless conductance is plotted versus system size for $T = 0.05$, $v_2 = 0$, and $V = 1.3$. Notice the log scale on the vertical axis. The solid line shows an exponential decay. In both panels, each point was obtained by averaging over 1000 disorder realizations.

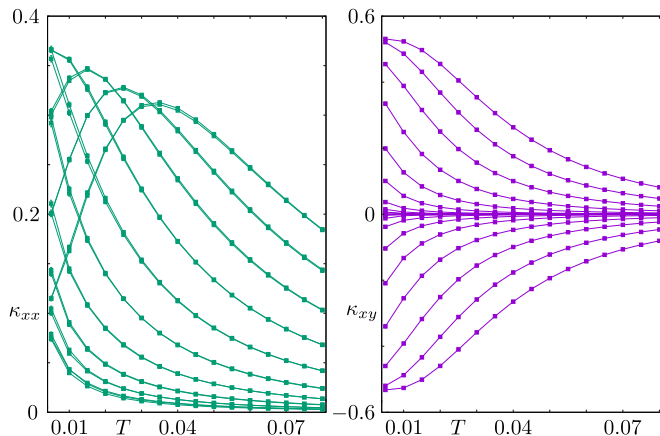


Figure 2. Average longitudinal (left) and transverse (right) dimensionless conductance plotted as a function of temperature. We use the same system size as in Fig. 3 of the main text, setting $v_1 = 1$ and $V = 1.3$. Each point is obtained by averaging over 1000 disorder realizations. Each curve corresponds to a different value of v_2 , from -0.1 to 0.1 in steps of 0.01 , and the solid lines are guides to the eye. In the left panel, larger values of κ_{xx} correspond to larger absolute values $|v_2|$, whereas in the right panel the larger κ_{xy} corresponds to larger v_2 .

T , the error bars of the conductance are obtained by recomputing the integral using transmission probabilities which are all one error bar above or one error bar below the mean.

Keeping a fixed system size, we observe that for small v_2 , both the longitudinal and the transverse dimensionless conductance decrease as a function of temperature, consistent with the formation of a finite-temperature plateau. This behavior is shown in Fig. 2, using the six terminal geometry discussed earlier. As mentioned in

the main text, conductance quantization improves with increasing temperature.

III. LOCALIZATION LENGTH

In the following, we estimate the energy dependence of the localization length in the framework of a nonlinear σ model [2]. At low energies, for which the system size is much smaller than the localization length but larger than the mean-free path, ℓ_0 , the renormalization group (RG) flow of the σ model proceeds as in class D, with a beta function $\beta(t) \equiv -dt/d \ln L$ given by

$$\beta_D(t) = t^2, \quad (3)$$

where the coupling constant $t = 1/(\pi P)$ is proportional to the inverse of the dimensionless conductance in the zero temperature limit, which is equivalent to the transmission probability P , computed in the cylinder geometry. This variable is usually denoted by g in σ model calculations, but here we refer to it as P to be consistent with previous notation. The solution of Eq. (3) is a logarithmically growing transmission probability,

$$P(L) = \text{const} + \frac{1}{\pi} \ln \frac{L}{\ell_0}, \quad (4)$$

consistent with the positive scaling obtained numerically in Fig. 1, left panel. To relate the above transmission probability to an energy scale, we use the RG equation for the second coupling constant, ε , whose bare value is the energy, E . This flow equation reads

$$\frac{d\varepsilon}{d \ln(L/\ell_0)} = (2 + t)\varepsilon. \quad (5)$$

Using the fact that the thermal metal transmission probability is large, meaning $t \ll 1$, we solve Eq. (5) to obtain $\varepsilon \simeq E(L/\ell_0)^2$. The class D RG flow towards larger L is therefore stopped by the energy, when the coupling constant $\varepsilon \sim 1$. After this point, the flow continues as in class A, corresponding to weak localization. Using that $\varepsilon \simeq E(L/\ell_0)^2$ is of order unity at this crossover point, we can estimate the crossover length scale at which the class A RG starts as

$$L_c = \ell_0 \left(\frac{1}{E} \right)^{1/2}, \quad (6)$$

corresponding to a transmission probability

$$P_c \equiv P(L_c) = \text{const} + \frac{1}{2\pi} \ln \left(\frac{1}{E} \right). \quad (7)$$

Starting from this value, the flow equation is now given by the negative beta function of class A:

$$\beta_A(t) = -t^3/2, \quad (8)$$

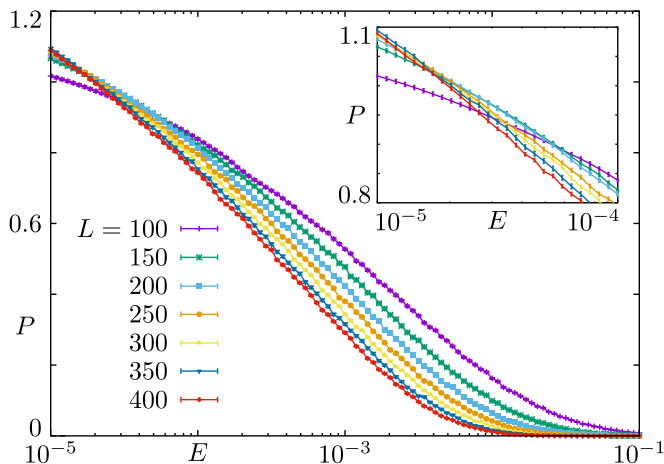


Figure 3. Average transmission probability computed at $v_2 = 0$, $V = 1.3$, plotted as a function of system size L and energy E (horizontal axis, logarithmic scale). Each data point was obtained using an $L \times L$ system, by averaging over 10^4 independent disorder realizations. The inset shows a closeup of the low-energy portion of the plot. At small E , the transmission probability first increases as a function of system size, and then becomes a decreasing function of L for large systems.

signaling localization. Solving Eq. (8) gives

$$P(L) = \sqrt{P_c^2 - \frac{1}{\pi^2} \ln \frac{L}{L_c}}. \quad (9)$$

The transmission probability now decreases as a function of system size from its initial value, P_c . To estimate the localization length, we use the approach of Ref. [3], which defines ξ as that length for which the transmission probability flows to a constant of order unity, $P(\xi) \sim 1$. If we neglect the constant term in Eq. (7), meaning that we consider the logarithm to be large, we obtain

$$\begin{aligned} \xi(E) &\simeq L_c \exp(\pi^2 P_c^2) \\ &= \frac{\ell_0}{\sqrt{E}} \exp\left(\frac{1}{4} \ln^2 \frac{1}{E}\right). \end{aligned} \quad (10)$$

The localization length has a sub-leading behavior which is power-law, $E^{-1/2}$. However, its asymptotic form is between a power law and an exponential: It grows like exponent of logarithm square. This result is consistent with a finite temperature conductance that decreases with system size, as shown in Fig. 1, right panel.

The localization length formula shown in the first line of Eq. (10) is consistent with discussion in Ref. [3] on how the localization length evolves when a magnetic field is added to an initially time-reversal symmetric, spin-orbit coupled system (class AII). There too, there was a crossover to class A in the RG flow, leading to a result equivalent to Eq. (10), albeit with different values of P_c and L_c .

We test the σ model prediction by numerically determining the transmission probability P at small energies

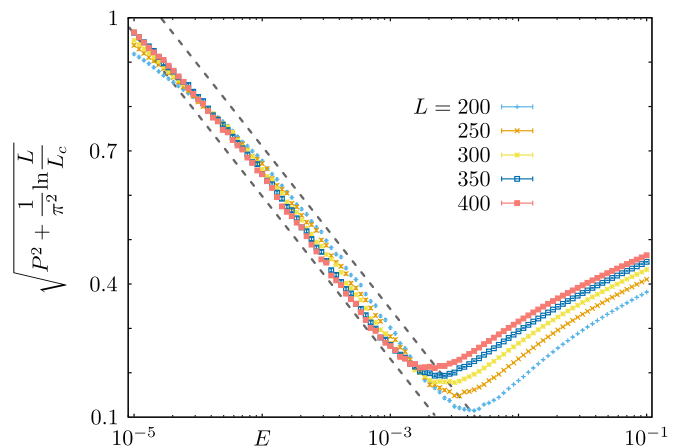


Figure 4. We rescale the data of Fig. 3 using the weak-localization result of Eq. (9). The value of L_c is given by Eq. (6) with $\ell_0 = 16$. The thick dashed lines show a $\ln(1/E)$ behavior with slope equal to $1/(2\pi)$, as predicted by Eq. (7).

and large system sizes, using a cylindrical geometry, setting as before a constant disorder strength $V = 1.3$. Figure 3 shows that, consistent with the previous discussion, the transmission probability is a non-monotonic function of L at small E . For small systems, we observe positive scaling, as expected in class D. For the largest system sizes, however, the scaling becomes negative, as for systems belonging to class A. The smaller the energy, the larger the values of L required before P becomes a decreasing function of system size.

We use Eq. (9) to rescale the numerically determined transmission probabilities shown in Fig. 3. This rescaling is shown in Fig. 4, where we plot the energy dependence of $\sqrt{P^2 + (1/\pi^2) \ln(L/L_c)}$ for system sizes $L \geq 200$, using L_c as in Eq. (6), with $\ell_0 = 16$. In the intermediate energy region, $10^{-4.5} \leq E \leq 10^{-3}$, the data points follow the analytical prediction of Eq. (6) (thick dashed lines). Both the $\ln(1/E)$ dependence and the slope of $1/(2\pi)$ are reproduced, thus validating the σ model results: weak antilocalization of class D and weak localization of class A. At the largest energies, $E \geq 10^{-2}$, we observe a sharp change of the behavior. This signals that the system is in the strong localization regime for these energies, i.e. transmission probability is very small and decays exponentially with system size. Finally, we note that for the smallest energies, $E \simeq 10^{-5}$, there is a deviation from a straight line behavior, which becomes smaller with increasing system size. This indicates that for the system sizes we can reach, $L \leq 400$, our smallest energies $E \simeq 10^{-5}$ are close to the crossover from class D to class A, such that the weak localization behavior of Eq. (9) has not yet fully set in.

IV. FINITE TEMPERATURE REGIMES

As mentioned in the main text, the longitudinal conductance Eq. (2) is an increasing function of system size in the limit of zero temperature, but shows an insulating behavior at high T . Here we study the behavior of κ_{xx} , identifying three temperature regimes, which depend on the relation between T and the two crossover energy scales introduced in the main text, E_L and E_c .

When $T < E_L$, the main contribution to the energy integral Eq. (2) comes from states with $E \sim T$ whose diffusion length L_E is larger than system size. These states are characterized by weak anti-localization, leading to the well known conductance scaling of a thermal metal, $\kappa_{xx} \simeq P(E=0) = \text{const} + (1/\pi) \ln(L/\ell_0)$, as shown in Eq. (4) and in the left panel of Fig. 1.

As temperature increases, a second scaling regime occurs when $E_L < T < E_c$. The integral Eq. (2) is then dominated by states with $E \sim T$ belonging to

this intermediate energy range, for which the transmission probability shows weak localization, as shown in Eq. (9). We therefore find $\kappa_{xx} \approx P(E=T) = (1/\pi) \sqrt{(1/4) \ln^2(1/T) - \ln(T^{1/2}L/\ell_0)}$, where we have used Eqs. (9) and (6). The thermal conductivity decreases logarithmically with increasing L or increasing T in this regime, which is a consequence of weak localization.

Finally, at temperatures $T > E_c$, the prefactor to the transmission probability in Eq. (2) is peaked at energies for which states are strongly localized, such that P is exponentially small. The main contribution to the energy integral then comes from $E \sim E_c(L)$, for which $P \sim 1$. This leads to the result $\kappa_{xx}(T, L) \sim [E_c(L)/T]^2$, where $E_c \approx \exp(-2\sqrt{\ln(L/\ell_0)})$ is obtained by setting $\xi(E_c) = L$ in Eq. (10). In this regime, the longitudinal conductivity decreases fast with increasing temperature or increasing length.

-
- [1] C. W. Groth, M. Wimmer, A. R. Akhmerov, and X. Waintal, “Kwant: a software package for quantum transport,” *New J. Phys.* **16**, 063065 (2014).
 [2] F. Evers and A. D. Mirlin, “Anderson transitions,” *Rev.*

- Mod. Phys.* **80**, 1355–1417 (2008).
 [3] I. V. Lerner and Y. Imry, “Magnetic-field dependence of the localization length in Anderson insulators,” *Europhys. Lett.* **29**, 49–54 (1995).